Research Article | Vol. 32, No. 7 / 25 Mar 2024 / Optics Express 11259
Optics EXPRESS

Wavelength division multiplexing based on the coupling effect of helical edge states in two-dimensional dielectric photonic crystals

LIU HE,[1] ZHIHAO LAN,[2,7] YUTING YANG,[3] QUN REN,[4,5] JIAN WEI YOU,[5] WEI E. I. SHA,[6] WU LIANG,[1,*] AND JIANQUAN YAO[1]

[1]Key Laboratory of Opto-Electronics Information Technology (Tianjin University), Ministry of Education, School of Precision Instruments and Opto-Electronics Engineering, Tianjin University, Tianjin 300072, China
[2]Department of Electronic and Electrical Engineering, University College London, Torrington Place, London WC1E 7JE, United Kingdom
[3]School of Materials Science and Physics, China University of Mining and Technology, Xuzhou 221116, China
[4]School of Electrical and Information Engineering, Tianjin University, Tianjin 300072, China
[5]State Key Laboratory of Millimeter Waves, School of Information Science and Engineering, Southeast University, Nanjing 210096, China
[6]Key Laboratory of Micro-Nano Electronic Devices and Smart Systems of Zhejiang Province, College of Information Science and Electronic Engineering, Zhejiang University, Hangzhou 310027, China
[7]lanzhihao7@gmail.com
[*]wuliang@tju.edu.cn

Abstract: Photonic topological insulators with topologically protected edge states featuring one-way, robustness and backscattering-immunity possess extraordinary abilities to steer and manipulate light. In this work, we construct a topological heterostructure (TH) consisting of a domain of nontrivial pseudospin-type topological photonic crystals (PCs) sandwiched between two domains of trivial PCs based on two-dimensional all-dielectric core-shell PCs in triangle lattice. We consider three THs with different number of layers in the middle nontrivial domain (i.e., one-layer, two-layer, three-layer) and demonstrate that the projected band diagrams of the three THs host interesting topological waveguide states (TWSs) with properties of one-way, large-area, broad-bandwidth and robustness due to coupling effect of the helical edge states associated with the two domain-wall interfaces. Moreover, taking advantage of the tunable bandgap between the TWSs by the layer number of the middle domain due to the coupling effect, a topological Y-splitter with functionality of wavelength division multiplexing is explicitly demonstrated exploiting the unique feature of the dispersion curves of TWSs in the three THs. Our work not only offers a new method to realize pseudospin-polarized large-area TWSs with tunable mode-width, but also could provide new opportunities for practical applications in on-chip multifunctional (i.e., wavelength division multiplexing) photonic devices with topological protection and information processing with pseudospin-dependent transport.

1. Introduction

Photonic topological insulators (PTIs) [1–9], motivated by the relevant electronic topological phenomena discovered in condensed matter physics [10–15], are systems that host topological boundary states robust against backscattering from imperfections, defects, disorder or sharp bends, offering great opportunities for achieving robust manipulation of electromagnetic (EM) waves, especially in applications for photonic integrated devices and on-chip communication. To date, based on the bulk-boundary-corner correspondence principle, a plethora of topological

#518922 https://doi.org/10.1364/OE.518922
Journal © 2024 Received 15 Jan 2024; revised 28 Feb 2024; accepted 2 Mar 2024; published 12 Mar 2024

Optics EXPRESS

photonic states (TPSs) have been theoretically proposed and experimentally demonstrated, such as photonic quantum Hall (QH) states [16–19], photonic quantum spin Hall (QSH) states [20–23], photonic quantum valley Hall (QVH) states [24–29], second-order photonic topological corner states [30–37], and so on. Each of them has unique feature in application for manipulating EM wave.

Recently, various methods to manipulate TPSs have been proposed and studied, such as multiband [38,39], finite-width waveguide states [40,41], cavity-waveguide-interaction [42,43], reconfiguration and recoding [44,45], wavelength division multiplexing [46,47], antichiral topological edge or surface states [48–51], and so forth, which enable novel applications for multi-functional photonic devices with built-in topological protection. Note that while the work of [46] proposed a design of wavelength division multiplexing devices based on varying the radius of rods in valley photonic crystals, and [47] based on rotating cylinder array in Zak-phase-characterized photonic crystals, we achieve this goal herein by exploiting the coupling effect between helical interface states in photonic crystals mimicking the QSH effect. Recently, Wang *et al* proposed and demonstrated topological one-way large-area waveguide states with uniformly distributed mode amplitude in the middle domain of a three-domain heterostructure based on the QH effect [19]. Moreover, Chen *et al* presented and demonstrated topological valley-locked waveguide states with tunable mode-width based on the QVH effect [52]. On the other hand, tunable finite-width waveguides based on the coupling effect between topological edge modes have also been realized [53,54]. These large-area waveguide states with tunable mode-width degree of freedom support high-capacity energy transport for applications in waveguide-based integrated photonic devices and circuits. However, these systems supporting TPSs with tunable finite mode-width are relatively complex for practical applications, e.g., the magneto-optical (MO) effect in [19] typically is weak in optical frequencies, and the lattice unit cells of photonic QSH or QVH insulators contain multiple photonic entities as in honeycomb lattice [20], kagome lattice [55], and stampfli-triangle lattice [56]. Hence here, we focus on using relatively simple photonic crystal (PC) unit cell to construct TPSs with tunable finite mode-width based on coupling effect of QSH states.

In this work, a kind of two-dimensional (2D) all-dielectric core-shell topological PCs in triangular lattice [57] is considered, and a novel application of the all-dielectric core-shell PCs for the construction of a topological heterostructure (TH) consisting of a domain of topologically nontrivial PCs sandwiched between two domains of trivial PCs is proposed. The projected band diagrams and resulting finite-width waveguide states based on the coupling effect between topological edge modes in three THs with different width of the middle domain (one-layer, two-layer, three-layer) are systematically investigated. Our simulation results show that such waveguide states possess the properties of multi-frequency and multi-mode, which depend on the number of layers in the nontrivial domain and the features of one-way, large-area, robustness and broad-bandwidth of these topological waveguide modes are explicitly demonstrated. Furthermore, exploiting the tunability of the dispersion and bandgap of the waveguide states due to the coupling effect, we design and realize a topological EM wave Y-splitter for wavelength division multiplexing based on the unique feature of the dispersion curves of these waveguide modes in the three THs. The THs proposed in this work not only offer a possibility to expand the working bandwidth and tune mode width, but also could be used in integrated multi-functional photonic devices and information processing with pseudospin-dependent transport.

2. 2D core-shell PCs

In this work, we consider a kind of 2D core-shell PCs in triangular lattice (with lattice constant $a = 1um$) made of all-dielectric core-shell silicon cylinders with relative permittivity $\varepsilon(r) = 11.7$ and outer and inner radii, r_1 and r_2, respectively, which are embedded in the background of air

Optics EXPRESS

(μ_0 and ε_0), as shown in Fig. 1(a). Note that we only consider the transverse-magnetic (TM) modes in this work, which have non-zero components of (H_X, H_Y, E_Z).

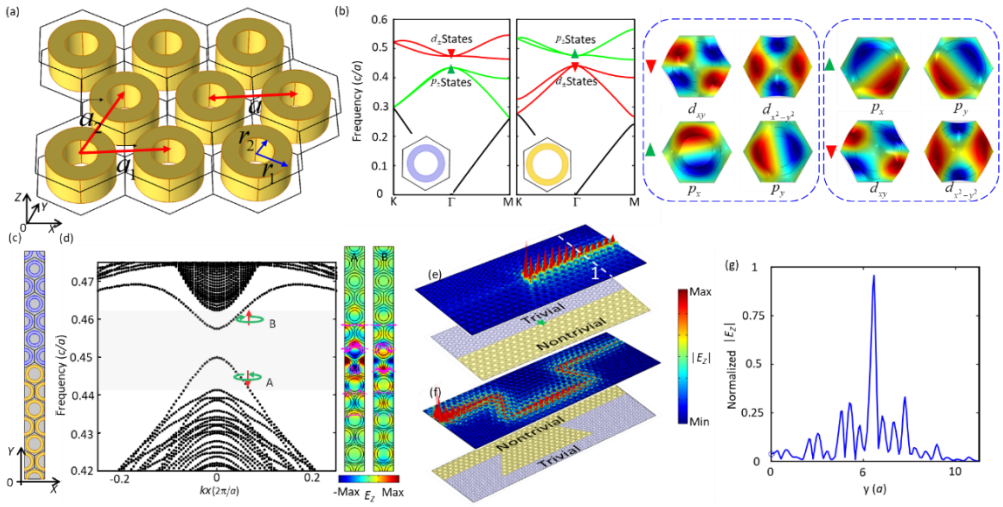

Fig. 1. (a) Schematic of the all-dielectric core-shell PCs in triangle lattice, where the outer and inner radii of the core-shell cylinder are r_1, r_2 respectively; vectors $\overrightarrow{a_1}$, $\overrightarrow{a_2}$ denote the two lattice vectors of the triangular lattice whereas the lattice constant a is $1\mu m$. (b) Photonic bulk band diagrams of the core-shell PCs with $r_1 = 0.4a$, $r_2 = 0.26a$ (left) and $r_1 = 0.45a$, $r_2 = 0.32a$ (right), respectively. The right two panels denote electric field (E_Z) profiles of the eigenmodes with pseudospin states $d_\pm$ and $p_\pm$. (c) Supercell of a domain-wall interface between trivial (blue) and nontrivial (golden) PCs. (d) Projected band diagram of the supercell in (c), and the right two panels represent eigenmode profiles with the pink arrows denoting the Poynting vectors, which rotate anticlockwise and clockwise around the domain-wall interface at eigenfrequencies f_A and f_B, respectively. (e) $|E_Z|$ distribution of unidirectional propagation of the helical edge states. (f) $|E_Z|$ distribution of robust propagation of the helical edge states in a waveguide structure with four sharp (60°) corners. (g) Normalized $|E_Z|$ distribution along the white dashed line in (e).

Similar to the mechanism for creating photonic QSH states of the Wu–Hu model [20] without breaking the time-reversal symmetry, the core-shell PCs, which are more convenient to fabricate and also are more compact, can also support pseudospin states $p_\pm = p_x \pm ip_y$ and $d_\pm = d_{x^2-y^2} \pm id_{xy}$, and a band inversion (thus topological phase transition) could be induced by tuning the radii of the core-shell cylinders [57]. To show this, bulk band diagrams of the core-shell PCs at different r_1 and r_2 are calculated and presented in Fig. 1(b). From the left bulk band diagram at $r_1 = 0.4a$ and $r_2 = 0.26a$ (with side length $L = \sqrt{3}/3a$ of the hexagonal lattice unit cell), one can see that the photonic eigenmodes below (above) the band gap at Γ are $p_\pm$ ($d_\pm$) states, thus the corresponding PC is trivial. On the other hand, at $r_1 = 0.45a$ and $r_2 = 0.32a$, as the right bulk band diagram of Fig. 1(b) shows, the photonic eigenmodes below (above) the band gap at Γ are $d_\pm$ ($p_\pm$), which are opposite to those of the previous case, indicating a band inversion and the corresponding PC is thus nontrivial in this case. The right two panels of Fig. 1(b) show the electric field profiles of the eigenmodes with pseudospin states $p_\pm$ and $d_\pm$. The topologically trivial and nontrivial PCs could be used to create photonic topological edge states at a domain-wall interface. To demonstrate this, the projected band diagram of a domain wall-interface between the trivial and nontrivial domains, whose supercell is depicted in Fig. 1(c), is calculated and presented in Fig. 1(d) using the finite element method (FEM), which shows that there are two QSH edge modes appearing within the bulk band gap. The pseudospin-momentum-locking unidirectional topological waveguide

Optics EXPRESS

states (TWSs) can be realized by using either a left-or right-circularly polarized excitation source (in the simulations, four dipoles with $\pi/2$ phase winding along the clockwise or anticlockwise direction are used as the circularly polarized excitation source). The pseudospin-momentum locking unidirectional propagation of these QSH edge modes is shown in Fig. 1(e) whereas in Fig. 1(f), the robustness of QSH edge modes against sharp bends during the propagation is demonstrated. To quantitatively characterize the energy intensity of the topological propagation, normalized electric field distribution along the dashed white line in Fig. 1(e) is plotted in Fig. 1(g) and the result shows that the wave is confined at the interface and decays dramatically away from it, which is very different from the tunable finite mode-width waveguide states as we will show in the following sections.

3. Models and discussions

3.1. Topological heterostructures

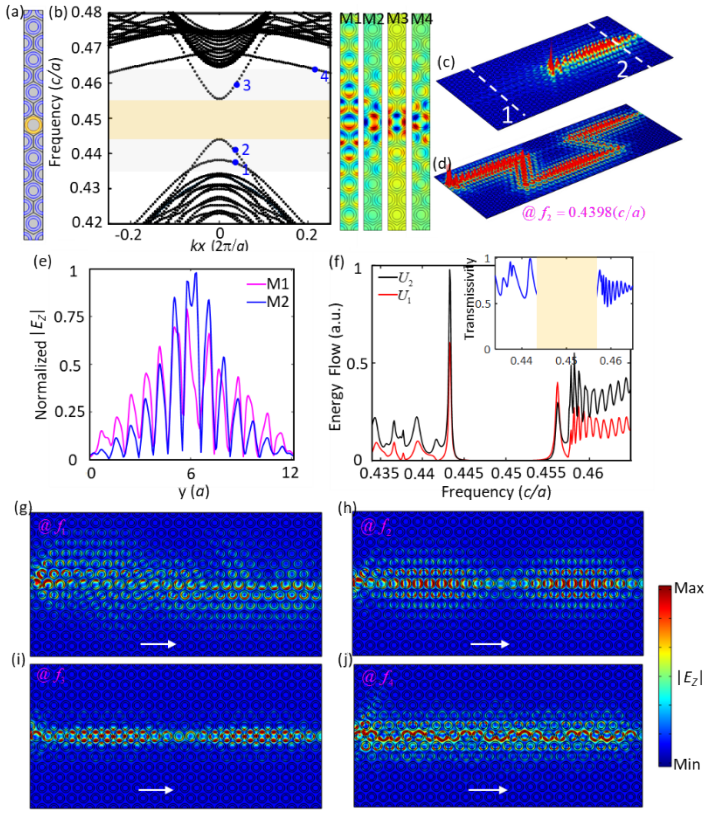

Fig. 2. (a) Supercell of the TH with NPZ-1. (b) Projected band diagram of the TH, where the right four panels represent eigenmode profiles of the four modes marked as 1, 2, 3 and 4 in the band diagram. (c) $|E_Z|$ distribution of unidirectional propagation of the large-area TWSs in the TH at frequency $f_2 = 0.4398(c/a)$. (d) $|E_Z|$ distribution of robust propagation of the large-area TWSs in the TH along a path with four sharp corners. (e) Normalized $|E_Z|$ profiles along the white dashed line 2 in (c) at frequencies $f_1 = 0.4292(c/a)$ and $f_2 = 0.4398(c/a)$. (f) Transmission spectrum of the large-area TWSs in the TH, where the inset shows the percentage of transmitted energy. (g)-(j) $|E_Z|$ distributions of four TWSs in the TH, where the white arrows denote the propagation direction of the EM waves.

Optics EXPRESS

Here we propose a novel application of the all-dielectric core-shell PCs discussed above for constructing THs, which consist of a domain of nontrivial PCs sandwiched between two domains of trivial PCs. The supercells of the THs are depicted in Figs. 2–4(a), where the middle zone of nontrivial PCs is called nontrivial PCs zone (NPZ) and these zones of nontrivial PCs with number of 1, 2, and 3 layers in the following are termed NPZ-1, NPZ-2 and NPZ-3, respectively. In specific, three THs with different layers of NPZ, i.e., NPZ-1, NPZ-2 and NPZ-3 will be constructed and their finite-width topological waveguide modes based on the coupling effect of helical edge states will be further analyzed and discussed.

3.2. TH with NPZ-1

We first calculate the projected band diagram of the TH with NPZ-1 and present the result in Fig. 2(b), from which one can see that there are four additional branches of edge states appearing within the bulk band gap. While the edge states within the light grey frequency region are TWSs, the light orange frequency region in the middle indicates a forbidden photonic band gap [40] because of the broken crystalline symmetry at the boundaries between different domains [20]. The appearance of the four additional branches of edge states can be understood from the fact that as one domain-wall interface between two domains with different topologies could host two pseudospin-related helical edge states, one can expect that there will be four pseudospin-related edge modes in our system as our TH has two topological domain-wall interfaces. To show the unique features of these TWSs, four eigenmodes, marked by 1, 2, 3, and 4 in the projected band diagram at $kx = 0.04(2\pi/a)$ and $kx = 0.21(2\pi/a)$, are shown in the right four panels of Fig. 2(b). From the results, one can see that while eigenmode 1 is an even symmetric mode with respect to the vertical mid-plane and eigenmodes 2, 3 are even symmetric modes with respect to the horizontal mid-plane, eigenmode 4 is an antisymmetric mode with respect to the vertical mid-plane, indicating a slow light state [58]. Moreover, while the E_Z eigenmode distributions of modes 2 and 3 are highly confined within the NPZ-1 due to the strong coupling and hybridization between the helical edge states associated with the two topological domain-wall interfaces, these of modes 1 and 4 are mainly distributed around the two domain-wall interfaces due to a weak coupling (see the Supplement 1 for the Poynting vector and $|E_Z|$ distributions of these four eigenmodes).

The topological properties of these TWSs in terms of propagation are further investigated. Fig. 2(c) shows the unidirectional excitation (at frequency f_2) and propagation properties of the TWSs, whose energy power flow during the propagation is highly concentrated in NPZ-1. To demonstrate the robust propagation of these TWSs against bends, we construct a waveguide structure with four sharp (60°) corners and the result in Fig. 2(d) shows that the wave can bypass the bends without being backscattered. These results clearly show that TWSs with robustness, and pseudospin-momentum locking unidirectional propagation could be realized in the TH with NPZ-1. To quantitatively characterize the transmission property of these TWSs, the normalized $|E_Z|$ distributions of the propagation along the white dashed line 2 in Fig. 2(c) at two different frequencies are plotted in Fig. 2(e), from which one can see that the normalized $|E_Z|$ distributions are mainly distributed within the NPZ-1 with width of a and two peaks appear around the two domain-wall interfaces, a property completely different from that of Fig. 1(g). To understand the transmission of the TWSs within the topological frequency window, their transmission spectrum is further studied. The EM wave energy that passes through the planes 1 and 2 (indicated by the white dashed lines in Fig. 2(c)) can be calculated by $U = 1/2 \int_l Re(\overrightarrow{E} \times \overrightarrow{H}*) \cdot dl$, from which we can define the percentage of transmitted energy as $U_2/(U_1 + U_2)$ and the resulting transmission spectrum is shown in Fig. 2(f). From the result, one can see that there are two transmission peaks outside the low-transmission region marked by the light orange frequency window for U_1 and U_2, indicating that the TWSs are forbidden within the photonic band gap. Inset of Fig. 2(f) shows the percentage of transmitted energy, exhibiting that there is a transmission peak around

Optics EXPRESS

the frequency of $0.443c/a$ and the average ratio of transmitted energy is approximately 70% in the whole topological frequency window (note that the light orange region is due to band gap effect). Finally, the electric field amplitude ($|E_Z|$) distributions of four pseudospin edge states during the propagation are shown in Figs. 2(g)-2(j), from which one can see that the electric field distributions are similar to those of the eigenmode distributions in Fig. 2(b), e.g., the TWSs are highly concentrated in the NPZ-1 at frequencies f_2 and f_3, whereas those of modes at frequencies f_1 and f_4 are mainly distributed around the up and down domain-wall interfaces and exhibit non-standing-wave-like patterns even if the mode at frequency f_4 is a slow light state because of the small slope of its dispersion curve. The above results demonstrate that multi-frequency and multi-mode properties are simultaneously realized in TH with NPZ-1 based on the coupling effect of helical edge states, which may offer a new opportunity for promising applications compared with those realized in [59–61].

3.3. TH with NPZ-2

The projected band diagram of TH with NPZ-2 (see Fig. 3(a) for its supercell) is calculated and presented in Fig. 3(b). Similarly, there are four additional branches of edge modes within the bulk band gap and the eigenmode profiles of four marked modes 1, 2, 3, and 4 at $kx = 0.04$ $(2\pi/a)$ are shown in the right panels of Fig. 3(b), which have similar features as those of TH with NPZ-1. However, the dispersion curve of eigenmode 4 is flatter than that of NPZ-1, indicating that the group index of this branch of modes is much larger and exhibits slow light behavior. Moreover, the dispersion curves of eigenmodes 3 and 4 intersect around $kx = 0.05$ $(2\pi/a)$, which means that eigenmodes at high (low) frequency are slow light states (guide modes) for kx less than $0.05(2\pi/a)$, whereas their propagation behaviors will be inverted for kx larger than $0.05(2\pi/a)$. Furthermore, one can also see that the light orange frequency band gap in the middle of the topological frequency window decreases due to the fact that the crystalline symmetry mismatch between different topological domains is mitigated by increasing the width of NPZ, and consequently, the bandwidth of TWSs increases.

Pseudospin-momentum locking unidirectional propagation and robustness of the propagation against sharp bends for the TWSs in TH with NPZ-2 are also demonstrated in Figs. 3(c) and 3(d). The normalized $|E_Z|$ profiles at two frequencies are plotted in Fig. 3(e), from which one can see that there are two maximum peaks and a deep drop in-between, which indicates that the EM wave is mainly distributed around the domain-wall interfaces and the average normalized $|E_Z|$ of TWSs in NPZ-2 is approximately 75% with mode width of $2a$. The transmission spectrum is further presented in Fig. 3(f) and the result shows that there are two transmission peaks outside the low-transmission region marked by the light orange frequency window for U_1 and U_2. The TWSs contribute more than 85% transmitted energy within the whole topological frequency window (see the inset). The drop within the light orange frequency region is narrower than that of the case in Fig. 2(f) because the tiny gap decreases due to the larger width of NPZ-2. Moreover, the transmission ratio approximately reaches up to 100% at four frequencies, which indicates that these branches of modes are more convenient for topological waveguiding. $|E_Z|$ distributions of the topological propagation for the four TWSs in the TH with NPZ-2, are given in Figs. 3(g)-3(j), from which one can see that the EM wave mainly concentrates around the domain-wall interfaces for frequencies f_1 and f_4, showing standing-wave-like patterns [54] (see Fig. 3(j)), whereas the TWSs at frequencies f_2 and f_3 are mainly distributed within NPZ-2, which are similar to those of NPZ-1.

3.4. TH with NPZ-3

For TH with NPZ-3, the projected band diagram is presented in Fig. 4(b) via simulating the supercell as depicted in Fig. 4(a). Interestingly, the light orange band gap as appearing in NPZ-1 and NPZ-2 within the topological frequency window vanishes when the width of the

Optics EXPRESS

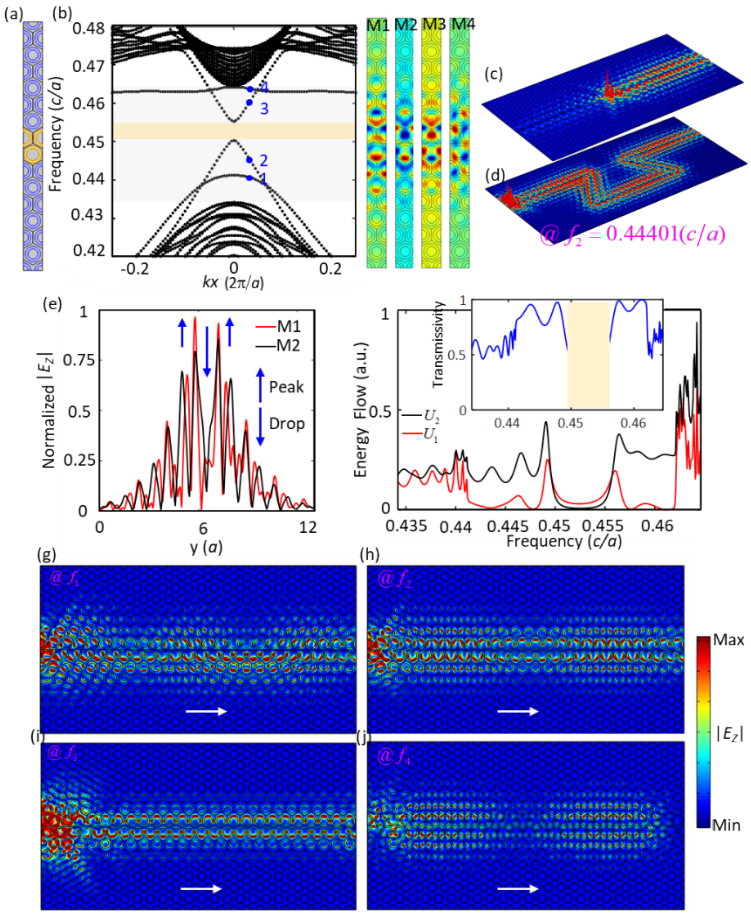

Fig. 3. (a) Supercell of the TH with NPZ-2. (b) Projected band diagram of the TH, where the right four panels represent eigenmode profiles of the four modes marked as 1, 2, 3 and 4 in the band diagram. (c) $|E_Z|$ distribution of unidirectional propagation of the large-area TWSs in the TH at frequency $f_2 = 0.44401(c/a)$. (d) $|E_Z|$ distribution of robust propagation of the large-area TWSs in the TH along a path with four sharp corners. (e) Normalized $|E_Z|$ profiles at frequencies $f_1 = 0.4405$ (c/a) and $f_2 = 0.44401(c/a)$. (f) Transmission spectrum of the large-area TWSs in the TH. (g)-(j) $|E_Z|$ distributions of four TWSs in the TH.

NPZ increases to $3a$ due to further reduction of the broken crystalline symmetry around the domain-wall interfaces. As such, the bandwidth of TWSs is further broadened, resulting in gapless TWSs. The pseudospin-momentum locking unidirectional propagation and robustness of the propagation against sharp bends for TWSs in TH with NPZ-3 are also demonstrated in Figs. 4(c) and 4(d). The normalized $|E_Z|$ profiles of two frequencies are plotted in Fig. 4(e), and the results exhibit two peaks and a drop in-between, which shows that the electric field is mainly distributed around the domain-wall interfaces and decreases dramatically within the up and down domains (see, e.g., the pink line). As the width of NPZ-3 increases, more peaks appear within NPZ-3, indicating that electric fields gradually decrease within the up and down domains, and $|E_Z|$ in the middle NPT (the drop) is approximately 50% whereas the average normalized $|E_Z|$ of TWSs originating from coupling modes is approximately 75% with mode width of $3a$. The transmission spectrum is shown in Fig. 4(f), from which one can see that the transmission of U_2 does not show a low transmission region with zero-transmission, while U_1

Optics EXPRESS

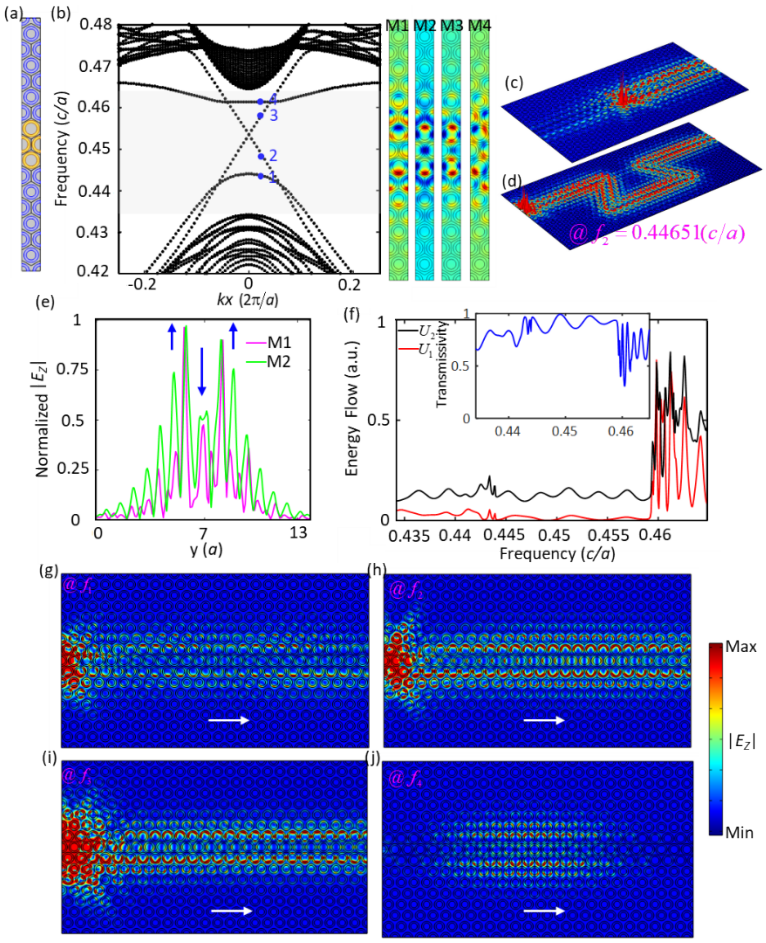

Fig. 4. (a) Supercell of the TH with NPZ-3. (b) Projected band diagram of the TH, where the right four panels represent eigenmode profiles of the four modes marked as 1, 2, 3 and 4 in the band diagram. (c) $|E_Z|$ distribution of unidirectional propagation of the large-area TWSs in the TH at frequency $f_2 = 0.44651(c/a)$. (d) $|E_Z|$ distribution of robust propagation of the large-area TWSs in the TH along a path with four sharp corners. (e)Normalized profiles at frequenciesf1 = 0.44297(c/a) and f2 = 0.44651(c/a). (f) Transmission spectrum of the large-area TWSs in the TH. (g)-(j) $|E_Z|$ distributions of four TWSs in the TH.

almost reaches to zero. The absence of a low transmission region with zero-transmission for U_2 indicates that the mismatch of crystalline symmetry at the domain-wall interfaces is very small. The inset shows that the TWSs contribute more than 90% transmitted energy within the whole topological frequency window. While a small drop with 85% transmission around frequency 0.453(c/a) between the two peaks could still be observed due to the fact that mismatch of crystalline symmetry at the domain-wall interfaces still exists, even if such a mismatch is small due to the large width of NPT-3 (the orange gap as in NPZ-1 and NPZ-2 is unnoticeable in the present scale). The $|E_Z|$ distributions of the topological propagation for the four TWSs in TH with NPZ-3 are shown in Figs. 4(g)-4(j), which show similar features as those of NPZ-1 and NPZ-2. Note that increasing the number of the middle layers to 4 and 5 will reduce the coupling effect further in NPZ-4 and NPZ-5 (see Supplement 1), where the small gap between the waveguide modes reappears. So the maximal bandwidth for the waveguide modes happens

Optics EXPRESS

for NPZ-3, which is due to the specific role of mode symmetry played in the coupling strength between the helical interface states.

4. Application

The above results show that the THs support a kind of TWSs with finite mode-width, pseudospin -momentum-locking unidirectional propagation, broad-bandwidth and robustness based on coupling effect of helical edge states. These TWSs due to the coupling effect of helical edge states provide new opportunities for waveguide-based photonic devices in on-chip communication. To show this application potential, in this section, we design and demonstrate the functionality of wavelength division multiplexing based on the unique dispersion curves of NPZ-1, NPZ-2 and NPZ-3.

To start, we first show the dispersion curves of the middle two branches of TWSs for NPZ-1, NPZ-2 and NPZ-3 in the same band gap, as shown in Fig. 5(a) and the design of a novel Y-splitter supporting the functionality of wavelength division multiplexing is shown in Fig. 5(b), where the different frequencies for the operation of the splitter are marked by A, B, and C in Fig. 5(a). The TWSs exist at frequency f_A for all three NPZs (i.e., NPZ-1, NPZ-2 and NPZ-3) because this frequency crosses all three dispersion curves L1, L2 and L3 (see Fig. 5(a)), and consequently the wave at this frequency can propagate in all three NPZs, see Fig. 5(c), where the white arrows denote energy flow directions. At a different frequency f_B, the TWSs can only propagate within NPZ-2 and NPZ-3 due to the band gap at this frequency for NPZ-1. The simulated propagation shown in Fig. 5(d) indeed confirms our design. Furthermore, at frequency f_C, the TWSs can only propagate within NPZ-3 and the propagation is forbidden within NPZ-1 and NPZ-2 due to the band gap associated with NPZ-1 and NPZ-2 at this frequency, where the simulated propagation shown in Fig. 5(e), again confirms the expected performance of the designed Y-splitter. The realization of the functionality of wavelength division multiplexing in our Y-splitter based on the coupling effect of pseudospin states with finite mode-width, provides a completely new way to realize photonic band shift and division compared to the method of tuning geometry of the material [46,47], such as tuning the radii of the dielectric cylinders or holes, and has a tremendous potential for novel applications in functional photonic integrated devices.

Furthermore, a kind of Y-splitters with different high-capacity energy distribution [62] could also be constructed in THs with NPZ-1, NPZ-2 or NPZ-3 due to their different mode widths, as demonstrated in Fig. 5(f)-5(h), where the bottom panels show the designed waveguide structures. These Y-splitters demonstrated in Fig. 5 can be used as different elementary structures for high-capacity energy transport, where on-demand applications of effective electric or magnetic energy transport in integrated photonic circuits could be realized by combining these basic functionalities. As the TWSs have inherent pseudospin-chirality locking property from the photonic spin Hall effect, splitting and transporting of these large-area waveguide modes could be controlled by the location of the chiral excitation source. For example, the local chirality (or directionality) [58,63] of the TWSs is zero at intersection of the three waveguide channels due to symmetry, and consequently, the TWSs can propagate along three different channels when the chiral source is located at the location with zero chirality.

Optics EXPRESS

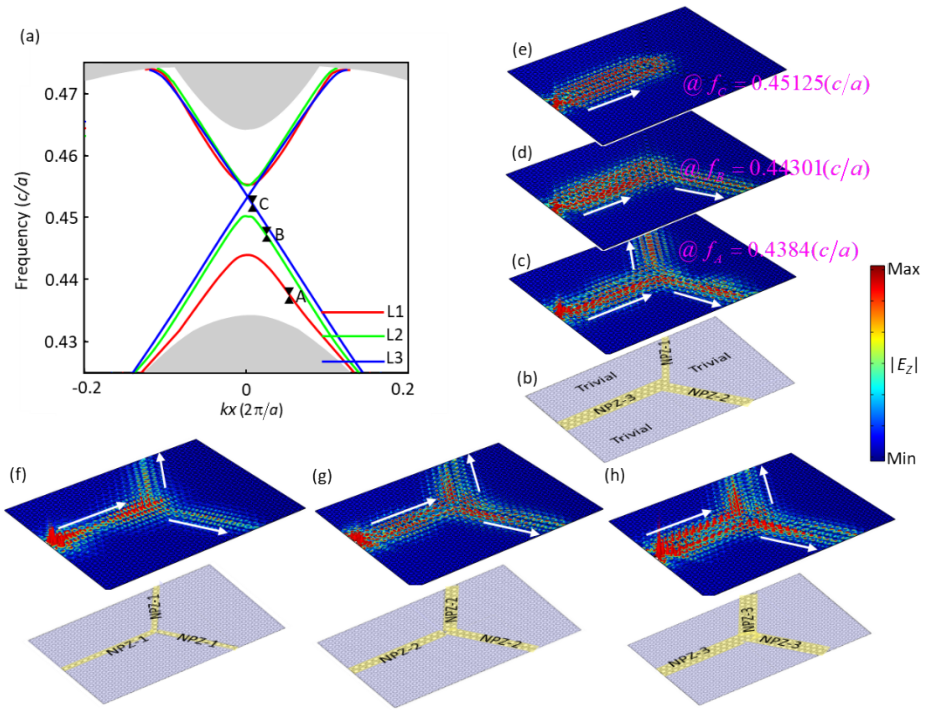

Fig. 5. Design and performance of a novel Y-splitter for wavelength division multiplexing. (a) Dispersion curves of TWSs for the three THs, where red, green and blue curves denote the dispersion curves of TWSs for NPZ-1, NPZ-2, and NPZ-3, respectively. (b) Schematic of the Y-splitter. (c)-(e) $|E_Z|$ distributions of propagation for TWSs in the Y-splitter at different frequencies of $f_A = 0.4348$(c/a), $f_B = 0.44301$(c/a), and $f_C = 0.45125$(c/a), respectively. (f)-(h) Performance of the Y-splitter structure with different mode width.

5. Conclusion

To conclude, we have proposed THs consisting of a domain of nontrivial PCs sandwiched between two domains of trivial PCs in all-dielectric core-shell PCs with triangle lattice. We studied in detail the topological properties of four branches of TWSs in three THs with NPZ-1, NPZ-2, and NPZ-3. TWSs with multi-frequency and multi-mode properties could be simultaneously realized in these THs, such as edge coupling modes, guide modes and slow light modes. The TWSs with pseudospin-momentum-locking unidirectional propagation, finite mode width, broad-bandwidth and robustness are realized and demonstrated in these THs based on the coupling effect of helical edge states. Moreover, we have proposed and designed a novel Y-splitter with functionality of wavelength division multiplexing based on the unique dispersion curves of the TWSs in these three THs. The structure of our design is easy to fabricate and has a compact nature in practice, which could provide a promising platform for topological photonic applications in waveguide-based integrated photonic devices, such as tunable finite mode-width waveguide, high-capacity energy splitter and transport, wavelength division multiplexing and multi-mode manipulation.

Funding. National Natural Science Foundation of China (U2230114); National Key Research and Development Program of China (2022YFA1203500).

Disclosures. The authors declare no conflicts of interest.

Optics EXPRESS

Data availability. Data underlying the results presented in this paper are not publicly available at this time but may be obtained from the authors upon reasonable request.

Supplemental document. See Supplement 1 for supporting content.

References

1. L. Lu, J. D. Joannopoulos, and M. Soljačić, "Topological photonics," Nat. Photonics **8**(11), 821–829 (2014).
2. A. B. Khanikaev and G. Shvets, "Two-dimensional topological photonics," Nat. Photonics **11**(12), 763–773 (2017).
3. T. Ozawa, H. M. Price, A. Amo, *et al.*, "Topological photonics," Rev. Mod. Phys. **91**(1), 015006 (2019).
4. D. Smirnova, D. Leykam, Y. Chong, *et al.*, "Nonlinear topological photonics," Appl. Phys. Rev. **7**(2), 021306 (2020).
5. Y. Ota, K. Takata, T. Ozawa, *et al.*, "Active topological photonics," Nanophotonics **9**(3), 547–567 (2020).
6. G. J. Tang, X. T. He, F. L. Shi, *et al.*, "Topological photonic crystals: physics, designs, and applications," Laser Photonics Rev. **16**(4), 2100300 (2022).
7. H. Price, Y. Chong, A. Khanikaev, *et al.*, "Roadmap on topological photonics," JPhys Photonics **4**(3), 032501 (2022).
8. J. You, Z. H. Lan, Q Ma, *et al.*, "Topological metasurface: From passive toward active and beyond," Photonics Res. **11**(3), B65–B102 (2023).
9. Z. H. Lan, M. L.N. Chen, F. Gao, *et al.*, "A brief review of topological photonics in one, two, and three dimensions," Rev. Phys. **9**(10), 100076 (2022).
10. D. Thouless, M. Kohmoto, M. P. Nightingale, *et al.*, "Quantized Hall conductance in a two-dimensional periodic potential," Phys. Rev. Lett. **49**(6), 405–408 (1982).
11. F. D. M. Haldane, "Model for a quantum hall effect without Landau levels: condensed-matter realization of the "Parity anomaly"," Phys. Rev. Lett. **61**(18), 2015–2018 (1988).
12. C. L. Kane and E. J. Mele, "Z_2 Topological order and the quantum spin Hall effect," Phys. Rev. Lett. **95**(14), 146802 (2005).
13. C. L. Kane and E. J. Mele, "Quantum spin Hall effect in graphene," Phys. Rev. Lett. **95**(22), 226801 (2005).
14. C. J. Wu, B. A. Bernevig, and S. C. Zhang, "Helical liquid and the edge of quantum spin Hall systems," Phys. Rev. Lett. **96**(10), 106401 (2006).
15. B. A. Bernevig and S. C. Zhang, "Quantum spin Hall effect," Phys. Rev. Lett. **96**(10), 106802 (2006).
16. F. D. Haldane and S. Raghu, "Possible realization of directional optical waveguides in photonic crystals with broken time-reversal symmetry," Phys. Rev. Lett. **100**(1), 013904 (2008).
17. Z. Wang, Y. D. Chong, J. D. Joannopoulos, *et al.*, "Reflection-free one-way edge modes in a gyromagnetic photonic crystal," Phys. Rev. Lett. **100**(1), 013905 (2008).
18. Z. Wang, Y. D. Chong, J. D. Joannopoulos, *et al.*, "Observation of unidirectional backscattering-immune topological electromagnetic states," Nature **461**(7265), 772–775 (2009).
19. M. D. Wang, R. Y. Zhang, L. Zhang, *et al.*, "Topological one-way large-area waveguide states in magnetic photonic crystals," Phys. Rev. Lett. **126**(6), 067401 (2021).
20. L. H. Wu and X. Hu, "Scheme for achieving a topological photonic crystal by using dielectric material," Phys. Rev. Lett. **114**(22), 223901 (2015).
21. Y. Yang, Y. F. Xu, T. Xu, *et al.*, "Visualization of a unidirectional electromagnetic waveguide using topological photonic crystals made of dielectric materials," Phys. Rev. Lett. **120**(21), 217401 (2018).
22. Y. Yang, Z. Gao, H. Xue, *et al.*, "Realization of a three-dimensional photonic topological insulator," Nature **565**(7741), 622–626 (2019).
23. L. He, Z. H. Lan, B. Yang, *et al.*, "Experimental observation of topological large-area pseudo-spin-momentum-locking waveguide states with exceptional robustness," Adv. Photon. Nexus **3**(01), 016009 (2024).
24. T. Ma and G. Shvets, "All-Si valley-Hall photonic topological insulator," New J. Phys. **18**(2), 025012 (2016).
25. X. D. Chen, F. L. Zhao, M. Chen, *et al.*, "Valley-contrasting physics in all-dielectric photonic crystals: Orbital angular momentum and topological propagation," Phys. Rev. B **96**(2), 020202 (2017).
26. J. W. Dong, X. D. Chen, H. Zhu, *et al.*, "Valley photonic crystals for control of spin and topology," Nat. Mater. **16**(3), 298–302 (2017).
27. X. T. He, E. T. Liang, J. J. Yuan, *et al.*, "A silicon-on insulator slab for topological valley transport," Nat. Commun. **10**(1), 872 (2019).
28. L. Zhang, Y. Yang, M. He, *et al.*, "Valley kink states and topological channel intersections in substrate-integrated photonic circuitry," Laser Photonics Rev. **13**(11), 1900159 (2019).
29. Y. H. Yang, Y. Yamagami, X. Yu, *et al.*, "Terahertz topological photonics for on-chip communication," Nat. Photonics **14**(7), 446–451 (2020).
30. F. Liu and K. Wakabayashi, "Novel topological phase with a zero Berry curvature," Phys. Rev. Lett. **118**(7), 076803 (2017).
31. X. D. Chen, W. M. Deng, F. L. Shi, *et al.*, "Direct observation of corner states in second-order topological photonic crystal slabs," Phys. Rev. Lett. **122**(23), 233902 (2019).
32. B. Y. Xie, G. X. Su, H. F. Wang, *et al.*, "Visualization of higher-order topological insulating phases in two-dimensional dielectric photonic crystals," Phys. Rev. Lett. **122**(23), 233903 (2019).
33. M. Kim and J. Rho, "Topological edge and corner states in a two-dimensional photonic su-schrieffer-heeger lattice," Nanophotonics **9**(10), 3227–3234 (2020).

Optics EXPRESS

34. Y. F. Chen, Z. H. Lan, and J. Zhu, "Inversely designed second-order photonic topological insulator with multiband corner states," Phys. Rev. Appl. **17**(5), 054003 (2022).
35. Y. F. Chen, F. Meng, Y. Kivshar, *et al.*, "Inverse design of higher-order photonic topological insulators," Phys. Rev. Res. **2**(2), 023115 (2020).
36. S. W. An, T. Liu, Y. Chen, *et al.*, "Routing edge states in an anisotropic elastic topological insulator," Phys. Rev. Appl. **18**(5), 054071 (2022).
37. Y. F. Chen, Z. H. Lan, J. Zhu, *et al.*, "Creating anisotropic topological phases within inversely designed photonic crystals," Opt. Laser Technol. **158**, 108865 (2023).
38. Q. Chen, L. Zhang, M. He, *et al.*, "Valley-Hall photonic topological insulators with dual-band kink states," Adv. Opt. Mater. **7**(15), 1900036 (2019).
39. Z. D. Zhang, S. Y. Yu, M. H. Lu, *et al.*, "Dual-band helical edge states and discrete Dirac vortices in solid-state elastic waves," Phys. Rev. Appl. **17**(3), 034029 (2022).
40. Y. Yang, X. Qian, L. Shi, *et al.*, "Observation and control of pseudospin switching in a finite-width topological photonic crystal," Opt. Express **30**(4), 5731–5738 (2022).
41. M. L. N. Chen, L. J. Jiang, Z. Lan, *et al.*, "Pseudospin-polarized topological line defects in dielectric photonic crystals," IEEE Trans. Antennas Propag. **68**(1), 609–613 (2020).
42. Y. Yang and Z. H. Hang, "Topological whispering gallery modes in two-dimensional photonic crystal cavities," Opt. Express **26**(16), 21235–21241 (2018).
43. Y. Zeng, U. Chattopadhyay, B. Zhu, *et al.*, "Electrically pumped topological laser with valley edge modes," Nature **578**(7794), 246–250 (2020).
44. X. X. Wang and X. Hu, "Reconfigurable topological waveguide based on honeycomb lattice of dielectric cuboids," Nanophotonics **9**(10), 3451–3458 (2020).
45. J. W. You, Q. Ma, Z. Lan, *et al.*, "Reprogrammable plasmonic topological insulators with ultrafast control," Nat. Commun. **12**(1), 5468 (2021).
46. X. R. Wang, Y. H. Han, H. Fei, *et al.*, "Design of wavelength division multiplexing devices based on tunable edge states of valley photonic crystals," Opt. Express **31**(9), 13933–13942 (2023).
47. Y. Ruan, X. Y. Qian, H. X. Wang, *et al.*, "Applications for wavelength division multiplexers based on topological photonic crystals," Photonics Res. **11**(4), 569–574 (2023).
48. P. Zhou, G. G. Liu, Y. Yang, *et al.*, "Observation of photonic antichiral edge states," Phys. Rev. Lett. **125**(26), 263603 (2020).
49. X. Xi, B. Yan, L. Yang, *et al.*, "Topological antichiral surface states in a magnetic Weyl photonic crystal," Nat. Commun. **14**(1), 1991 (2023).
50. J. W. Liu, F. L. Shi, K. Shen, *et al.*, "Antichiral surface states in time-reversal-invariant photonic semimetals," Nat. Commun. **14**(1), 2027 (2023).
51. Y. T. Yang, D. J. Zhu, Z. H. Hang, *et al.*, "Observation of antichiral edge states in a circuit lattice," Sci. China Phys. Mech. Astron. **64**(5), 257011 (2021).
52. Q. Chen, L. Zhang, F. Chen, *et al.*, "Photonic topological valley-locked waveguides," ACS Photonics **8**(5), 1400–1406 (2021).
53. Y. T. Fang, H. Q. He, and J. X. Hu, "Transforming unidirectional edge waveguide into unidirectional air waveguide," IEEE J. Sel. Top. Quantum Electron. **22**(2), 293–301 (2016).
54. H. X. Wang, H. Chen, J. H. Jiang, *et al.*, "Tunable edge states in reconfigurable photonic crystals," J. Appl. Phys. **126**(19), 93105 (2019).
55. X. Zhu, H. X. Wang, C. Xu, *et al.*, "Topological transitions in continuously deformed photonic crystals," Phys. Rev. B **97**(8), 085148 (2018).
56. B. Yan, J. L. Xie, E. Liu, *et al.*, "Topological Edge State in the Two-Dimensional Stampfli-Triangle Photonic Crystals," Phys. Rev. Appl. **12**(4), 044004 (2019).
57. L. Xu, H. X. Wang, Y. D. Xu, *et al.*, "Accidental degeneracy in photonic bands and topological phase transitions in two-dimensional core-shell dielectric photonic crystals," Opt. Express **24**(16), 18059–18071 (2016).
58. L. He, Q. Ren, J. W. You, *et al.*, "Coexistence of slow light states and valley-polarized kink states in all-dielectric valley photonic crystals with triangular lattice," Opt. Laser Technol. **167**, 109790 (2023).
59. X. Xi, K. P. Ye, and R. X. Wu, "Topological photonic crystal of large valley Chern numbers," Photonics Res. **8**(9), B1–B7 (2020).
60. B. Yan, Y. Peng, A. Shi, *et al.*, "Pseudo-spin-valley coupled topological states protected by different symmetries in photonic crystals," Opt. Lett. **47**(8), 2044 (2022).
61. B. Yan, Y. Peng, J. Xie, *et al.*, "Multifrequency and multimode topological waveguides in Stampfli-triangle photonic crystal with large valley Chern numbers," arXiv, arXiv:2104.14142, (2022).
62. L. He, H. Y. Ji, Y. J. Wang, *et al.*, "Topologically protected beam splitters and logic gates based on two-dimensional silicon photonic crystal slabs," Opt. Express **28**(23), 34015–34023 (2020).
63. Z. H. Lan, J. W. You, Q. Ren, *et al.*, "Second-harmonic generation via double topological valley-Hall kink modes in all-dielectric photonic crystals," Phys. Rev. A **103**(4), L041502 (2021).